Published OnlineFirst March 1, 2011; DOI: 10.1158/1541-7786.MCR-10-0469

Molecular Cancer Research

Angiogenesis, Metastasis, and Tumor Micronenvironment

HIF-1–Dependent Stromal Adaptation to Ischemia Mediates *In Vivo* Tumor Radiation Resistance

David L. Schwartz[1,2], James Bankson[3], Luc Bidaut[3], Yi He[1], Ryan Williams[4], Robert Lemos[4], Arun Kumar Thitai[2], Junghwan Oh[1], Andrei Volgin[2], Suren Soghomonyan[2], Hsin-Hsien Yeh[2], Ryuichi Nishii[2], Uday Mukhopadhay[2], Mian Alauddin[2], Ioseb Mushkudiani[2], Norihito Kuno[1], Sunil Krishnan[1], William Bornman[4], Stephen Y. Lai[5], Garth Powis[4], John Hazle[3], and Juri Gelovani[2]

Abstract

Purpose: Hypoxia-inducible factor 1 (HIF-1) promotes cancer cell survival and tumor progression. The specific role played by HIF-1 and tumor–stromal interactions toward determining tumor resistance to radiation treatment remains undefined. We applied a multimodality preclinical imaging platform to mechanistically characterize tumor response to radiation, with a focus on HIF-1–dependent resistance pathways.

Methods: C6 glioma and HN5 human squamous carcinoma cells were stably transfected with a dual HIF-1 signaling reporter construct (dxHRE-tk/eGFP-cmvRed2XPRT). Reporter cells were serially interrogated *in vitro* before and after irradiation as monolayer and multicellular spheroid cultures and as subcutaneous xenografts in *nu/nu* mice.

Results: *In vitro*, single-dose irradiation of C6 and HN5 reporter cells modestly impacted HIF-1 signaling in normoxic monolayers and inhibited HIF-1 signaling in maturing spheroids. In contrast, irradiation of C6 or HN5 reporter xenografts with 8 Gy *in vivo* elicited marked upregulation of HIF-1 signaling and downstream proangiogenic signaling at 48 hours which preceded recovery of tumor growth. *In situ* ultrasound imaging and dynamic contrast-enhanced (DCE) MRI indicated that HIF-1 signaling followed acute disruption of stromal vascular function. High-resolution positron emission tomography and dual-contrast DCE-MRI of immobilized dorsal skin window tumors confirmed postradiotherapy HIF-1 signaling to spatiotemporally coincide with impaired stromal vascular function. Targeted disruption of HIF-1 signaling established this pathway to be a determinant of tumor radioresistance.

Conclusions: Our results illustrate that tumor radioresistance is mediated by a capacity to compensate for stromal vascular disruption through HIF-1–dependent proangiogenic signaling and that clinically relevant vascular imaging techniques can spatially define mechanisms associated with tumor irradiation. *Mol Cancer Res; 9(3); 259–70. ©2011 AACR.*

Introduction

Tumor hypoxia predicts for tumor radioresistance and poor clinical outcome (1–3). Tumor cells which survive hypoxic stress are selected for reduced apoptotic potential, increased angiogenic signaling, enhanced metastatic capability, and greater resistance to radiotherapy and cytotoxic chemotherapy. The biological cornerstone of these hypoxia-specific stress responses is the hypoxia-inducible factor 1 (HIF-1) transcription factor (4). Given prosurvival and angiogenic effects of HIF-1, targeted inhibition of HIF-1 signaling has generated interest as a target for therapeutic modulation of radioresistance (5). We have previously confirmed tumor radiosensitization with selective pharmacologic blockade of tumor HIF-1 signaling in glioma, squamous cell, and pancreatic cancer cell lines (6, 7). Nonetheless, the temporal dynamics and compartmental sources (e.g., tumor cells vs. stromal vessels) of HIF-1–mediated proangiogenic responses to radiation have not been elucidated; serial *in situ* imaging would be an ideal means by which to identify such responses to guide future studies to identify optimal timing of HIF-1–targeted intervention with radiation delivery.

Tumor vessels are distinct from their normal counterparts by virtue of their dependence on prosurvival stimulatory cytokines such as VEGF (8). Tumor cells upregulate VEGF

Authors' Affiliations: Departments of [1]Radiation Oncology, [2]Experimental Diagnostic Imaging, [3]Imaging Physics, [4]Experimental Therapeutics, and [5]Head and Neck Surgery, The University of Texas M.D. Anderson Cancer Center, Houston, Texas

Note: J. Bankson and L. Bidaut contributed equally to this work. J. Hazle and J. Gelovani contributed equally to this work.

Corresponding Author: David L. Schwartz, Department of Radiation Medicine, Hofstra North Shore-LIJ School of Medicine, 270-05 76th Ave. New Hyde Park, NY 11040. Phone: 516-470-7190; Fax: 516-470-8445. E-mail: dschwartz3@nshs.edu

doi: 10.1158/1541-7786.MCR-10-0469

Published OnlineFirst March 1, 2011; DOI: 10.1158/1541-7786.MCR-10-0469

expression in direct response to irradiation (9), but the relative contribution of direct stimulation of VEGF signaling in tumor cells by radiation versus indirect ischemic HIF-1 stimulation of VEGF expression in tumor cells through radiation-induced disruption of vascular supply is not clear. Recent data (10) suggested that radiation can induce ischemia-reperfusion and reoxygenation-dependent HIF-1 signaling which prompts proangiogenic cytokine secretion, enhances endothelial viability, and improves xenograft survival following irradiation which is sensitive to pharmacologic inhibition of HIF-1. However, the mechanistic interpretation of results from this study remains unconfirmed.

In this study, we investigated the mechanism and spatiotemporal dynamics of HIF-1–mediated responses to radiation in C6 glioma and HN5 squamous carcinoma HIF-1 reporter cell lines (11, 12). In contrast to the reoxygenation-related mechanisms suggested previously, our results indicate that tumor cell HIF-1 signaling is closely associated with microenvironmental ischemia. We first observed in monolayer cultures and multicellular spheroids that radiation minimally impacts or inhibits HIF-1 transcriptional activity. In contrast, *in vivo* irradiation of C6 and HN5 tumor xenografts with 8 Gy led to hypoxia-dependent upregulation of HIF-1 signaling at 48 hours. Immunohistochemical (IHC) staining and novel high-resolution, HIF-1–specific positron emission tomography (PET) and dual-tracer dynamic contrast-enhanced (DCE) MRI of an immobilized dorsal skin window tumor model confirmed that delayed upregulation of HIF-1 signaling and VEGF production in the tumor cell compartment was induced by disruption of stromal vascular function. *In vivo* pharmacologic or genetic knockdown of HIF-1 signaling suppressed adaptive tumor revascularization and abrogated tumor regrowth following irradiation. These findings establish a foundation for refinement of rationally designed preclinical HIF-1–targeting strategies and indicate that clinically available imaging techniques such as DCE-MRI and ultrasonography promise immediate relevance toward streamlining translation of these strategies into clinical trials.

Materials and Methods

Reporter cell culture and shRNA knockdown

C6 rat glioma cells were obtained from American Type Culture Collection, whereas HN5 human squamous cell lines were provided by Dr. Luka Milas (Department of Experimental Radiation Oncology, M.D. Anderson Cancer Center). C6 (designated #4C6) and HN5 cells were stably transfected with a dual HIF-1 signaling reporter construct (dxHRE-tk/eGFP-cmvRed2XPRT), which has a bifunctional genetic reporter consisting of herpes simplex virus 1-thymidine kinase (HSV-tk) and green fluorescent protein (GFP) under transcriptional control of the hypoxia response element (12). This construct generated intranuclear GFP signal and HSV-tk gancyclovir analogue retention under the control of 8× tandem hypoxia response elements. Cytoplasmic red fluorescent protein (RFP) signal under CMV promoter control provided baseline beacon signal. For experiments in hypoxic conditions, culture flasks and plates were incubated for noted times and sequences at 37°C in humidified hypoxic air (1% O_2, 5% CO_2, and 94% N_2) using an *in vivo* Hypoxic Workstation 400 with a Ruskin hypoxic gas mixer (Biotrace International). Human HIF-1α short hairpin (shRNA) oligonucleotide (ggcttaccatcagctatttctcaagagaaaatagctgatggtaagcctc) was cloned into the pSingle-tTS-shRNA vector (Clontech) at *Hin*dIII and *Xho*I sites. The recombinant vector was transfected using Lipofectamine 2000 per manufacturer's protocol into HN5-HIF-1 reporter cells. Stable, clonal transformants were selected with G418. HN5 reporter cells transfected with pSingle-tTS-scrambled shRNA vector were created as controls.

Monolayer radiation treatments/treatments/GFP quantification

Cells were grown on 96-well plates at 1×10^4 cells/well for 24 hours, treated with 0 to 16 Gy single-fraction irradiation per ^{137}Cs unit at 5.8 Gy/min ± concurrent exposure to 200 μmol/L $CoCl_2$. GFP/RFP signal ratio, to correct inducible GFP signal for baseline reporter activity, was determined by fluorescence spectrometry with an automated TECAN Freedom Evo microplate reader and normalized according to viable cell density as quantified by WST1 uptake, as previously described (6).

Spheroid radiation treatment/treatments/GFP quantification/immunohistochemistry

#4C6 multicellular spheroids were generated from 2×10^3 cells in 96-well V-bottomed plates as previously described (12). Individual spheroids were transferred into agarose-coated 96-well flat-bottomed plates and were treated with 0 to 16 Gy single-fraction irradiation as described earlier for monolayer cultures 2 days after plating ± concurrent 200 μmol/L $CoCl_2$ treatment. Cell viability confirmation and GFP/RFP signal ratio measurement were also conducted as described earlier. GFP signal was normalized to constitutive RFP signal and was scaled from a baseline value of 1 at day 0 of each experiment. Digital photomicrographs were taken with a CCD camera–mounted Olympus IX81/FV1000 Fluoview confocal microscope. For IHC analysis, 3 spheroids were serially sectioned in their entirety (3–4 adjacent sections, 4-μm thickness) at 50-μm intervals. IHC staining, digital microphotography, and image analysis were done as indicated later for tumor tissue.

Clonogenic survival assays

HN5-HRE-HIF-shRNA cells were grown to 70% confluence with or without treatment with 1 μg/mL doxycycline for 72 hours. During the final 24 hours, cells were incubated at 21% O_2 (normoxia) or 1% O_2 (hypoxia, via chamber) and irradiated with a ^{137}Cs source (5.8 Gy/min) under atmospheric conditions. Cells were assayed for colony formation by replating at specified numbers into 6-well plates in the drug-free medium. The cells were immediately plated after irradiation, maintained for 12 days in normoxia,

Published OnlineFirst March 1, 2011; DOI: 10.1158/1541-7786.MCR-10-0469

and stained with 0.5% crystal violet in absolute ethanol. Colonies with more than 50 cells were counted. Clonogenic survival curves were constructed from 3 independent experiments.

In vivo limb and dorsal tumor window xenografts

A total of 2×10^6 #4C6 or HN5 reporter cells were implanted subcutaneously into the right forelimb of *nu/nu* mice. Xenografts were allowed to grow to approximately 250 mm^3 over 2 weeks prior to treatment and imaging. HN5-HIF-1-shRNA knockdown xenografts were implanted in an identical fashion. Tumor volumes were determined from digital caliper measurements by the following formula: tumor volume (mm^3) = $\pi/6$ [(short axis in $mm)^2 \times$ (long axis in mm)]. For the dorsal tumor window tumor model, MRI-compatible Duralon dorsal flank skin windows were secured with nonabsorbable suture, and 2×10^5 #4C6 reporter cells were injected subcutaneously within the window. Tumors grew for approximately 12 days to a volume of 150 mm^3 prior to treatment and imaging. All animals were handled and treated according to Institutional Animal Care and Utilization Committee guidelines.

Animal irradiation

Irradiated tumors received 8-Gy single-fraction treatment with a ^{60}Co unit at 1.8 Gy/min, with custom head and body shielding.

Tumor tissue immunohistochemistry and image analysis

Control and radiated tumors were collected at indicated time points. Pimonidazole (Pimo) at a concentration of 25 mg/mL was injected intravenously into animals 60 minutes prior to sacrifice. Tumors were routinely fixed in 4% formaldehyde/PBS, processed into paraffin, and then sectioned at 4-μm thickness. To ensure adequate sampling, 4 tumors for each treatment condition were collected, bisected, and then serially sectioned (10 adjacent sections, 4-μm thickness) at 100- to 150-μm intervals in either direction. IHC staining for individual epitopes was done on a Vision Biosystems BondMax automated slide stainer (VBS) and nuclei were visualized by staining with hematoxylin. Pimo adducts were stained using a fluorescein isothiocyanate (FITC)-labeled monoclonal antibody, followed by a horseradish peroxidase–conjugated anti-FITC polyclonal antibody (Hypoxyprobe-1 Plus; Chemicon). Tumor vasculature was visualized with a polyclonal CD105 antibody (R&D Systems). HIF-1α was detected with a monoclonal antibody from BD Transduction Laboratories, Ki-67 and GFP were detected with polyclonal antibodies from Abcam, and VEGF and cleaved caspase-3 were detected with polyclonal antibodies from R&D Systems and Cell Signaling, respectively. Specificity of all staining was confirmed with nonspecific control antibodies. High-resolution images were acquired using a Nikon E90i microscope with automated stage and a Roper CoolSNAP K4 digital camera (Roper Scientific) through a plan-apo 4× objective. Sections were imaged in their entirety, manually registered with Photoshop CS2 software to permit direct overlay with staining from adjacent slices, and analyzed on a pixel-by-pixel basis for signal intensity and overlap by using Compix SimplePCI (Hamamatsu Corp) image analysis software. Intensity cutoffs were empirically determined for each antigen on the basis of the control nonspecific antibody slides and used for every image from that antibody series. Percent pixel-to-pixel GFP and VEGF signal overlap with Pimo was quantified as 100 × (number of GFP-VEGF and Pimo-positive pixels)/(total number of GFP-VEGF–positive pixels) for all analyzed sections and pooled for statistical analysis.

Micro-PET whole animal imaging

Repetitive, noninvasive whole animal molecular-genetic PET imaging of HIF-1 signaling was made possible through selective intracellular retention of radiolabeled reporter substrate 2′-^{18}F-fluoro-2′-deoxy-5-ethyl-1-β-D-arabinofuranosyluracil (^{18}F-FEAU), which was synthesized using a modified no-carrier added procedure (13). For each time point and study condition, 9 to 10 mice were injected IV with 100 μCi (100 μL) of ^{18}F-FEAU. Fifteen-minute static images were acquired under inhalation anesthesia on a commercial micro-PET system (R4; Concorde Microsystems). Images were reconstructed using the ordered subset expectation maximization algorithm. Regional radioactivity concentrations (kBq/cm^3 or μCi/cm^3) for ^{18}F-FEAU were estimated from regions of interest (ROI) drawn around the tumor or organ on transaxial slices from the reconstructed image sets. Tumor tracer uptake was normalized to background muscle uptake in the contralateral shoulder and quantified as a maximal tumor-to-muscle ratio (TMR) averaged from 3 separate levels on axial projection, measured in triplicate with standardized 3 to 7 pixel diameter 2-dimensional ROIs. Pooled results from each study animal group were reported as mean values ± standard error.

Ultrasound imaging

Ultrasound imaging of xenografts was carried out with a Vevo 770 system (VisualSonics), using a single-element transducer with 40-MHz center frequency. Power Doppler settings were held constant at 25 dB Power Doppler gain, 5 kHz pulse repetition rate, 2.5 mm/s wall filter with 2 mm/s scan speed. Initial imaging of tumor was carried out in B-mode to discriminate tumor boundaries, and Doppler images were acquired for a manually delineated ROI encompassing the entire tumor. Vascular area in tumor was calculated by color pixel density, defined as the ratio of the number of color pixels (i.e., pixels with a Doppler measurable flow) to the total number of pixels within the ROI.

MRI

Serial single-tracer DCE-MRI data from a 6-mouse xenograft study cohort treated with 8-Gy single-dose irradiation was acquired using a 4.7T Biospec USR47/40 small animal imaging system (Bruker Biospin MRI, Inc.) with a 35-mm linear volume resonator and 60-mm microimaging gradients. A 3-plane RARE imaging sequence was used to confirm animal positioning, and coronal T_2-weighted

Published OnlineFirst March 1, 2011; DOI: 10.1158/1541-7786.MCR-10-0469

RARE images [TE/TR 70/4,000 ms, field of view (FOV) 4 × 3 cm^2, matrix 256 × 192, RARE factor 12] were used for tumor localization. Axial T_1-weighted spin-echo images (TE/TR 8.5 ms/700 ms, FOV 4 × 3 cm^2, matrix 256 × 192) were acquired before and after administration of 0.2 mmol/kg gadopentetate dimeglumine (Gd-DTPA, Magnevist; Berlex Laboratories), an Food and Drug Administration–approved T_1-reducing contrast agent. DCE-MRI data were acquired using a multislice fast spoiled gradient-recalled echo sequence (TE/TR 1.4/40 ms, FOV 4 × 3 cm^2, matrix 128 × 96, 35 degrees excitation angle, 3.8 s/repetition, 100 repetitions). Baseline images were collected for 1 minute prior to injection of the contrast agent. A generalized kinetic model (14, 15) was applied to manually segmented data by using Matlab (The Mathworks).

Dorsal skin window tumor imaging

Mice were immobilized under inhalation anesthesia on a CT (computed tomography)/MRI/PET/ultrasound-compatible sled with a built-in MR surface coil and ^{68}Ge point-source fiducial markers adjacent to window frames for *post hoc* image localization and registration. Fluctuations in signal relaxation (T_2*) due to susceptibility differences (often attributed to changes in oxygen saturation) were measured using a multi-echo gradient-echo sequence (TE_{min} 4.5 ms, 7.23-ms interval between each of 12 echoes, TR 1,500 ms, FOV 2 × 1.5 cm^2, matrix 256 × 256). A dual-tracer DCE-MRI acquisition (16) was implemented using poly(l-glutamic acid) Gd-DTPA (PG-Gd-DTPA; ref. 17) and Magnevist. After 1 minute of T_1-weighted baseline scans by using a fast spoiled gradient-echo sequence (TE/TR 1.65 ms/75 ms, FOV 2 × 1.5 cm^2, matrix 128 × 96, 50 degrees excitation angle), 0.06 mmol/kg PG-Gd-DTPA was injected with a tail vein catheter. Five minutes later, 0.2 mmol/kg Magnevist was injected, and enhancement was monitored for 3 more minutes. All data were segmented manually and analyzed using Matlab. HIF-1 signaling detection with ^{18}F-FEAU-PET was conducted as described earlier. To facilitate registration, 3-dimensional (3D) micro-CT imaging was obtained with an eXplore micro-CT system (GE Healthcare). All imaging was completed within 4 hours. PET was first registered to the reference anatomic CT through a gross rigid transformation to match marker sets and major structures such as body outlines that are visible on both modalities. This initial registration was then further refined through the multiresolution iterative maximization of a normalized mutual information cost function (18). A similar process was used to register MR to CT, albeit with a high-resolution FOV that was limited to anatomy that was visible within the physical tumor window. Once registered together, the PET, CT, and MR data sets were fused together, processed, and visualized (19) to localize and compare PET uptakes and MR parametric maps in relation to structural anatomy.

Statistical testing

Significance of difference between pooled results from study groups was measured via unpaired 2-sided Student's *t* test using GraphPad v.4.

Results

In situ functional imaging shows tumor cell HIF-1 radiation response to be unique to the *in vivo* setting

Radiation minimally impacted or inhibited tumor cell HIF-1 signaling in the absence of vascularized stroma. There was no change in HIF-1–dependent GFP signal in normoxic #4C6 and HN5-HIF-1 reporter monolayers following escalating doses up to 8 Gy, although a decrease in HIF-1 signal was seen uniquely in #4C6 cells 72 hours following irradiation at 16 Gy (Fig. 1A). Irradiation of chemically hypoxic (200 μmol/L $CoCl_2$) cells with irradiation at up to 16 Gy did not alter HIF-1 activity, indicating that radiation does not directly impact ongoing tumor HIF-1 signaling response to hypoxic stress (Fig. 1B). Radiation treatment *in vitro* modestly impacted downstream VEGF signaling in the absence of upstream HIF-1 induction. VEGF mRNA remained stable and soluble protein expression increased incrementally in normoxic #4C6 or HN5 monolayers treated with irradiation at 8 Gy (data not shown). Hypoxic #4C6 or HN5 monolayers showed an expected increase in VEGF protein expression within 48 hours, which was unaffected by irradiation at 8 Gy, consistent with HIF-1 expression results.

To further model the microenvironment of hypoxic tumors, #4C6 cells were cultured as 3D spheroids measuring at least 500 μm in diameter. Confocal microscopy revealed hypoxia/HIF-1–induced GFP signal in the central region of spheroids, extending outward to a depth of approximately 100 μm from the surface. Single-fraction irradiation inhibited GFP expression in maturing spheroids in a dose-dependent manner (Fig. 1C and D). Quantified IHC staining of spheroids confirmed reduction of centralized HIF-1 and downstream VEGF signal in spheroids treated with irradiation at 4 to 8 Gy (Fig. 1E). Treatment with irradiation at up to 16 Gy did not inhibit preexisting HIF-1 signaling or VEGF expression in spheroids treated with 200 μmol/L $CoCl_2$ (Fig. 1C).

Although direct effects of radiation on tumor cell HIF-1 signaling appeared modest, we observed profound HIF-1 tumor cell signaling responses within intact vascularized tumors. *Nu/nu* mice ($n = 9$) bearing #4C6 xenografts were serially imaged for HIF-1 transcriptional activity with ^{18}F-FEAU-PET over 8 days. Irradiation at 8 Gy induced delayed, incremental upregulation of HIF-1 activity in tumor cells at 48 hours (mean maximum TMR of ^{18}F-FEAU accumulation = 4.51 ± 0.23 standard error vs. 3.97 ± 0.11 for controls, $P < 0.05$; Student's *t* test), which subsequently peaked at day 6 posttreatment (mean maximum TMR = 7.85 ± 0.24 vs. 5.77 ± 0.18 for controls, $P < 0.005$). HIF-1 upregulation was heterogeneous and discretely localized to viable peripheral regions within tumors (Fig. 2A). The marked upregulation of HIF-1 activity observed in irradiated tumors at day 6 subsequently decreased by day 8 to levels comparable with controls (mean maximum TMR = 5.64 ± 0.22 vs. 5.21 ± 0.17 for controls, P = n.s.). HIF-1 upregulation in irradiated tumors was accompanied by refractory, albeit slowed, tumor growth (Fig. 2B). ^{18}F-FEAU-PET

Published OnlineFirst March 1, 2011; DOI: 10.1158/1541-7786.MCR-10-0469

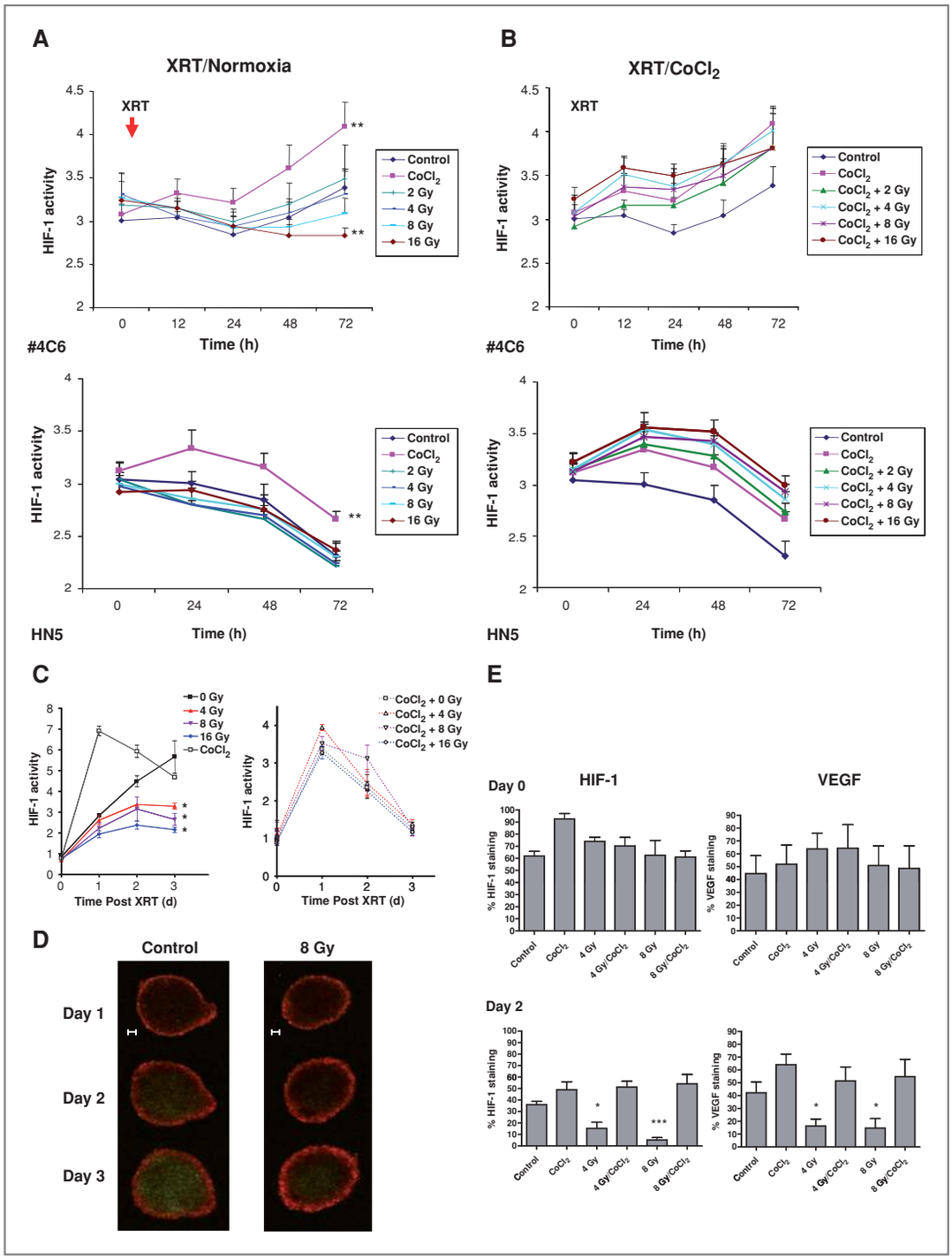

Figure 1. A, radiation inhibits HIF-1 signaling in aerobic #4C6 and HN5 monolayer cultures in a dose-dependent fashion but does not impact HIF-1 signaling in hypoxic monolayers. HIF-1 activity (GFP signal normalized to constitutive RFP signal, reported as mean values ± SD) over time following radiation (timing of treatment designated "X") in normoxic and $CoCl_2$ treated (timing of treatment designated "C") monolayers. B, normalized HIF-1 signal at 72 hours postirradiation in normoxic and hypoxic monolayers plotted against radiation dose. C, radiation inhibits initial development of, but not preestablished, hypoxia signaling within #4C6 spheroid cultures. HIF-1–dependent GFP signal normalized to constitutive RFP signal, reported as mean values ± SD. All statistical comparisons are with controls at identical time points; *, $P < 0.05$. D, serial fluorescence photomicrographs of representative spheroids over time at designated time points. Bar, 100 μm. E, spheroids were treated with 0, 4, or 8 Gy single-fraction radiation 2 days after plating, ± concurrent 200 μmol/L $CoCl_2$. IHC staining results for HIF-1 and VEGF expression for each treatment condition were pooled (~30 images total) and reported as mean % staining of total tissue area ± SD. All statistical comparisons are with baseline controls at designated time points; *, $P < 0.05$; ***, $P < 0.001$.

Published OnlineFirst March 1, 2011; DOI: 10.1158/1541-7786.MCR-10-0469

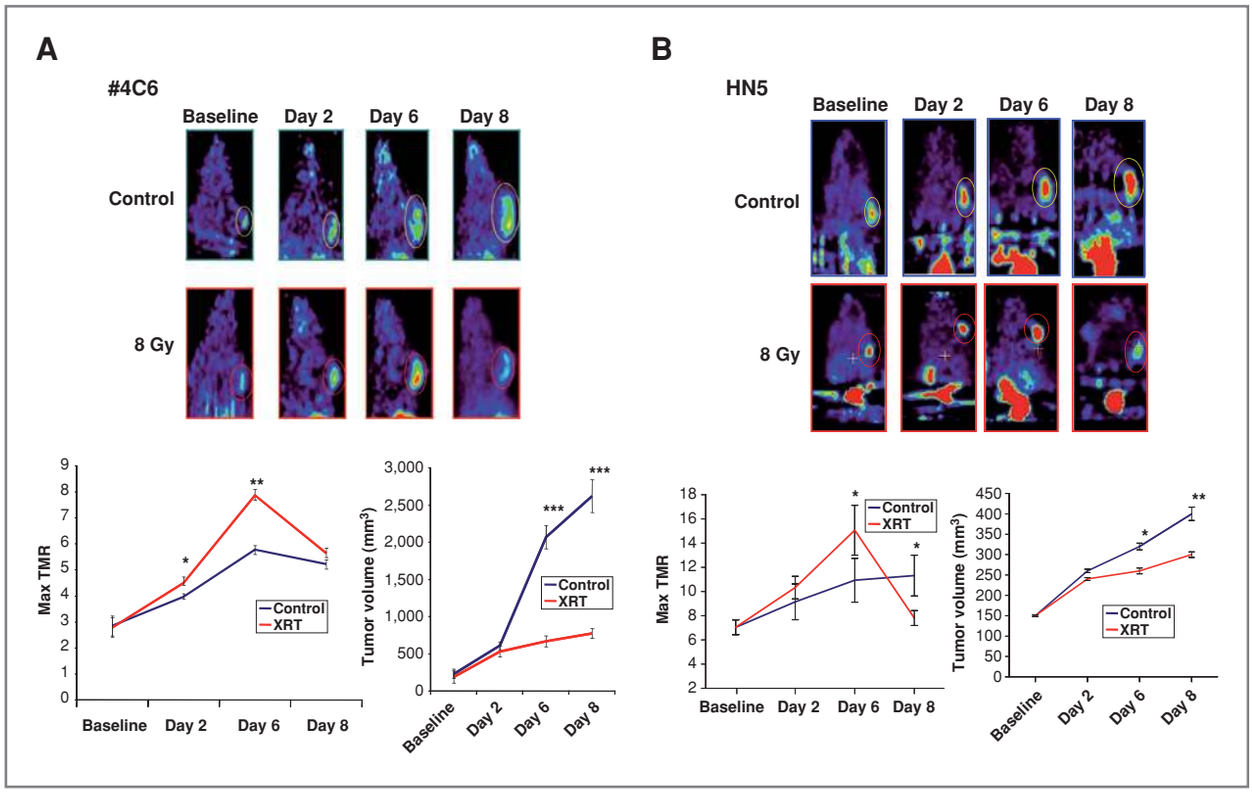

Figure 2. Radiation induces delayed HIF-1 Gy signaling in (A) #4C6 and (B) HN5 xenografts. Top, whole animal ^{18}F-FEAU-PET imaging, with tumors indicated by ovals. Bottom left, pooled quantification of 18F-FEAU TMR (*, $P < 0.05$, between treatment groups; **, $P < 0.005$ between treatment groups). Bottom right, volumetric tumor growth over time, reported as mean tumor volume values ± standard error; ***, $P < 0.001$.

imaging of irradiated HN5 reporter xenografts ($n = 6$) confirmed similar findings (Fig. 2B).

Stromal vessel dysfunction and ischemic insult are closely associated with postradiation HIF-1 tumor cell signaling

We interrogated temporal kinetics and spatial associations between postradiation microenvironmental stress and tumor cell HIF-1 signaling in greater detail by IHC staining. #4C6 tumors treated with irradiation at 8 Gy showed an acute reduction in overall tumor HIF-1–dependent GFP reporter and VEGF expression at 4 hours (Fig. 3). A concomitant decrease in Pimo staining showed that, at this stage, tumors were less hypoxic. This was associated with metabolic and proliferative arrest in tumor cells rather than improved tumor perfusion, as evidenced by reduced ^{18}F-FDG uptake, bromodeoxyuridine, and Ki-67 tumor proliferation indices and ^{18}F-2′-deoxy-2′-flouro-5-methyl-1-β-D-arabinofuranosyluracil proliferation tracer uptake at 24 hours postradiation (data not shown). However, localized, discrete areas of persistent HIF-1–dependent GFP signaling and VEGF signal were observed, closely correlating with areas with Pimo retention (Fig. 3A). Quantitative pixel-by-pixel analysis of GFP and VEGF IHC images coregistered with Pimo IHC images confirmed that high baseline spatial overlap of GFP (44.84% ± 11.85%) and VEGF (38.85% ± 11.15%) signal with regions of physical hypoxia remained unchanged 48 hours following radiation treatment (XRT) (43.68% ± 11.18% for GFP and 34.60% ± 8.84% for VEGF, P = n.s., Fig. 3C), arguing against a functional association between reoxygenation events and HIF-1 signaling. Vascular endothelial cells (EC) positive for both CD105 and cleaved caspase-3 were seen exclusively in regions devoid of GFP and VEGF signals.

In situ ultrasound imaging and DCE-MRI of irradiated #4C6 xenografts functionally corroborated these findings. Irradiation at 8 Gy led to transient disruption of tumor blood flow on power Doppler ultrasonography ($n = 6$ per cohort). This was observed within 24 hours following completion of radiation (74.9% ± 1.1% decrease, $P < 0.001$), with a notable loss of blood flow within the central and superficial portions of xenografts away from extrinsic host soft tissues (Fig. 4A). This reduced blood flow was accompanied by an increase in globally quantified measures of vascular permeability, shown by increased average volume transfer constant [K^{trans} (min^{-1}), a rate constant which is potentially value-limited by either blood flow or vessel permeability] values from single-tracer DCE-MRI

Published OnlineFirst March 1, 2011; DOI: 10.1158/1541-7786.MCR-10-0469

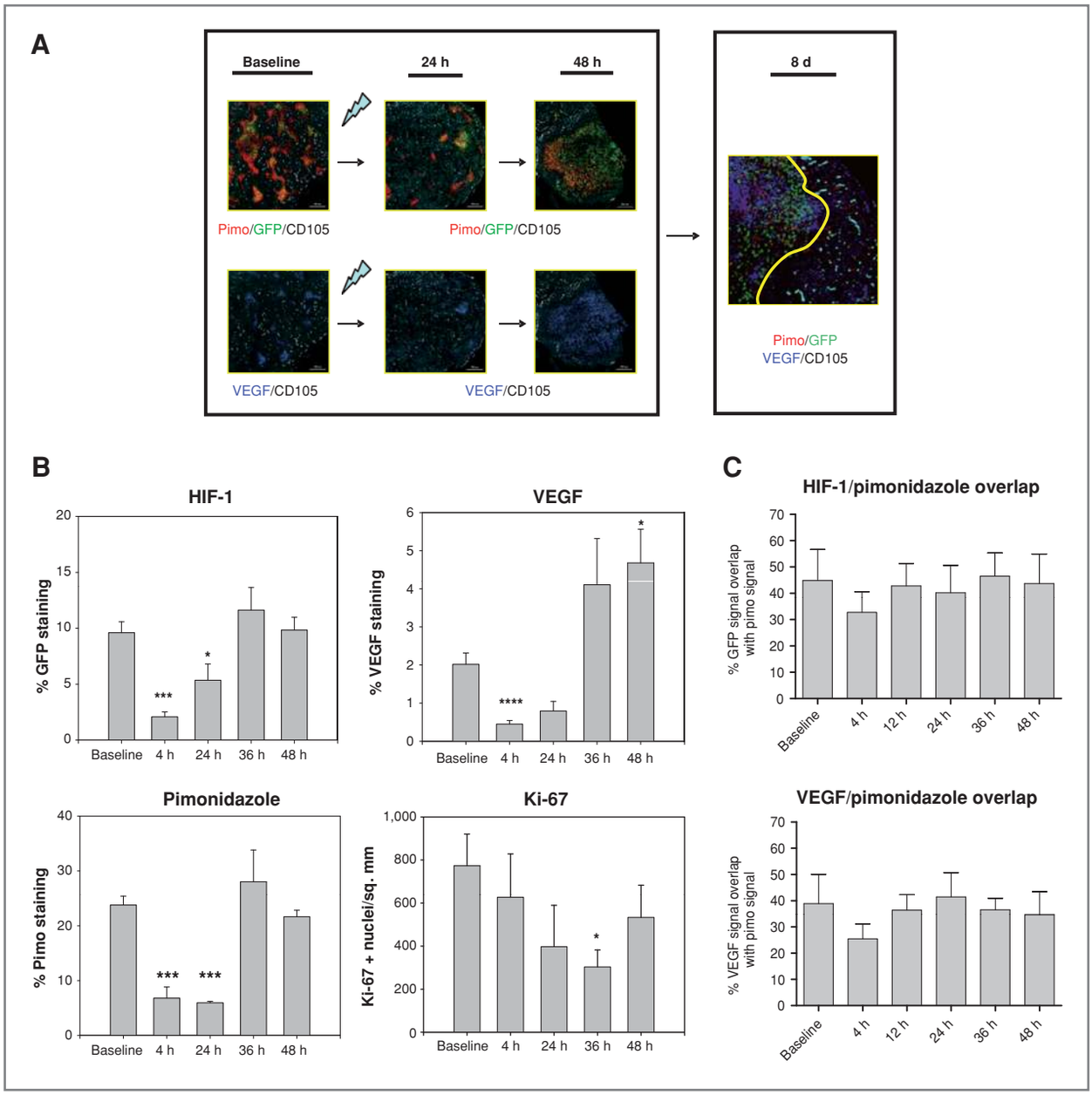

Figure 3. Postradiation *in vivo* HIF-1 signal induction results from stromal vessel dysfunction and ischemic insult. A, serial 4× photomicrographs of IHC i i staining for HIF-1, Pimo, VEGF, and CD105$^+$ microvessels in control and irradiated #4C6 xenograft tumors. Images from 24 hours posttreatment tissue samples illustrate focal radioresistant HIF-1–dependent GFP signal and VEGF expression in regions retaining Pimo 24 hours posttreatment. By 8 days posttreatment, normalization of HIF-1 transcriptional activity, VEGF expression, and Pimo staining are seen in revascularized regions populated with CD105$^+$ vessels. However, tumor adaptation is not uniform; areas of Pimo retention, HIF-1–dependent GFP signal, and VEGF protein colocalize to focal devascularized regions (to the left of the revascularized region demarcated by the solid yellow line), recapitulating the heterogeneous tumor microenvironment seen at baseline. B, quantification of % staining of total tissue area over time in pooled tissue sections, reported as mean values ± SD. All statistical comparisons are with baseline pretreatment values; *, $P < 0.05$; ***, $P < 0.001$. C, quantified pixel-by-pixel analysis of % spatial overlap ± SD between GFP/VEGF signal and Pimo at baseline and following irradiation.

mapping (578% ± 57% increase, $P < 0.005$) within 24 hours (Fig. 4B). Acutely increased K^{trans} values were distributed heterogeneously within nonnecrotic regions, consistent with regionalized loss of vascular integrity and blood flow within remaining functional stroma. Both blood flow and K^{trans} values began to return toward baseline at 48 hours, in concert with the timing of HIF-1 upregulation.

Published OnlineFirst March 1, 2011; DOI: 10.1158/1541-7786.MCR-10-0469

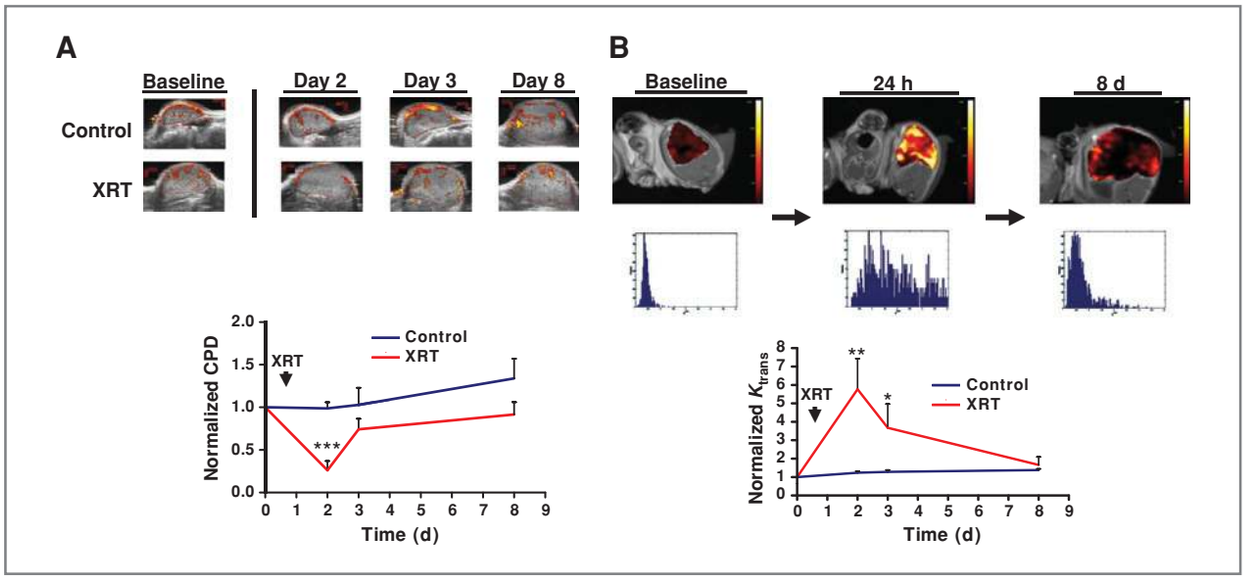

Figure 4. A, serial color power Doppler imaging of a representative #4C6 xenograft shows transient loss of central and peripheral tumor vascular flow by 24 hours postradiation, followed by early stromal vessel recovery 48 hours posttreatment. Statistical comparisons of pooled results at each posttreatment time point are with baseline pretreatment values; ***, $P < 0.001$. B, serial single-tracer DCE-MRI mapping of K^{trans} values in a representative #4C6 xenograft shows increased K^{trans} values by 24 hours postradiation, consistent with loss of vascular integrity. Corresponding K^{trans} value distribution histograms are shown below each image. K^{trans} values normalize toward baseline values by 7 days posttreatment. Statistical comparisons of pooled results at each time point are with baseline findings, as reported as mean values ± SD; *, $P < 0.05$; **, $P < 0.005$.

High-resolution multimodality imaging localizes postradiation HIF-1 signaling to regions of impaired vascular function

We used coregistered PET, dual high/low-molecular-weight tracer DCE-MRI, MR angiography, and MR relaxometry in a dorsal skin window tumor system to colocalize postradiation HIF-1 tumor signaling to regions of stromal dysfunction and low oxygen tension. Fiducial landmarks and mechanical immobilization provided by the dorsal skin window frame permitted high-fidelity image coregistration. Dual-tracer DCE-MRI provided reproducible estimation of vessel permeability in the absence of vascular input data from major vessels within the FOV of the surface coil. PET imaging of #4C6 skin window tumors ($n = 6$) reproduced earlier findings of tumor HIF-1 signaling 2 days postradiation. Overlap between HIF-1–dependent ^{18}F-FEAU signal and low-molecular-weight contrast delivery to the extravascular compartment (Fig. 5) confirmed close colocalization of HIF-1 signaling with postradiation tumor microvessel disruption. The timing and location of these imaging biomarkers corroborate a direct functional association between adaptive HIF-1 tumor cell signaling and abrupt ischemic microenvironmental stress following irradiation.

Postradiation HIF-1 tumor cell signaling precedes tumor stromal recovery and is a necessary determinant of tumor radiation resistance

Consistent with our imaging results, IHC staining confirmed regionalized ischemic upregulation of HIF-1 transcriptional activity and VEGF expression 36 to 48 hours following irradiation, most notably in previously perfused peripheral tumor regions (Fig. 3A and B). Upregulation of HIF-1 and VEGF signaling was accompanied by the reemergence of a proliferating Ki-67$^+$ tumor cell subpopulation. By 1 week postirradiation, CD105$^+$ vessels returned to regions of reduced HIF-1 and VEGF signaling, consistent with physiologically relevant reperfusion. Vascular function returned toward baseline on power Doppler imaging and DCE-MRI by day 7 posttreatment (Fig. 4A and B).

Taken together, these findings indicate that ischemia-driven stromal responses are critical to tumor radiation resistance and provide a mechanistic rationale for targeted disruption of HIF-1. We have previously confirmed tumor radiosensitization with targeted pharmacologic blockade of tumor HIF-1 signaling with the selective HIF-1 inhibitor PX-478 in C6, HN5, and pancreatic cancer cell lines (6, 7). Power Doppler imaging and DCE-MRI showed that PX-478 abolishes HIF-1–dependent postradiotherapy tumor stromal recovery and that constitutive expression of downstream angiogenic signals can restore refractory tumor vessel function during drug exposure. To confirm specificity of these findings, we introduced conditionally inducible human HIF-1 shRNA into HN5 reporter cells, which yielded inhibition of HIF-1 and downstream VEGF expression in response to hypoxic stimulation (1% O_2 for 24 hours; Fig. 6A and B). HIF-1 shRNA induction yielded a modest direct

Published OnlineFirst March 1, 2011; DOI: 10.1158/1541-7786.MCR-10-0469

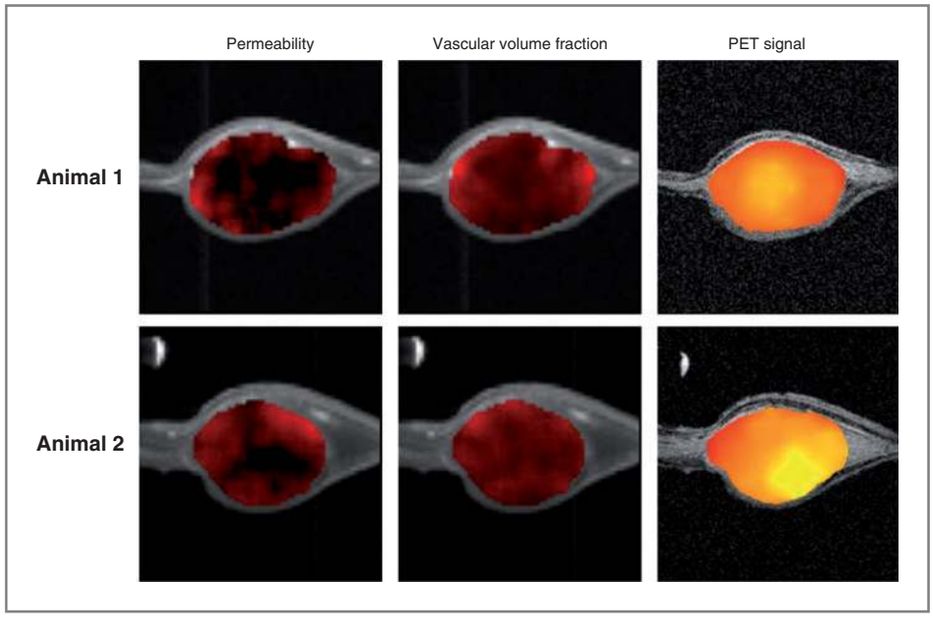

Figure 5. Dual-tracer DCE-MRI parametric maps of vascular function coregistered with HIF-1–specific PET imaging of an immobilized dorsal skin window C6#4 reporter tumor model 48 hours following 8-Gy irradiation. Columns, from left to right, (1) low-molecular-weight contrast–dependent permeability mapping, (2) high-molecular-weight PG-Gd-DTPA contrast–dependent vascular volume fraction mapping, and (3) HIF-1–dependent ^{18}F-FEAU retention imaged mid-F-at plane within 2 representative tumors (top and bottom rows), with regions of impaired microvessel low-molecular-weight tracer delivery to the extravascular compartment spatially corresponding with regions of elevated HIF-1–dependent signal.

effect on hypoxic cells, with a sensitizer enhancement ratio at 0.2 surviving fraction of 1.35 versus 1.01 seen in 1% and 21% O_2 conditions, respectively (Fig. 6C). Induction of HIF-1 shRNA *in vivo* in HN5 xenografts inhibited HIF-1 expression detected by IHC/Western blotting and also downstream HIF-1 signal detected by GFP expression (not shown). Identical to PX-478, induction of HIF-1 shRNA (5 mg doxycycline via oral gavage × 3 days) prior to 8-Gy irradiation of HN5 xenografts led to stable tumor growth delay, not seen following either treatment alone (Fig. 6D).

Discussion

Hypoxia is associated with tumor radiation resistance (3, 20–22) and is classically described as a modifier of the physical effects of radiation on tumor cell DNA integrity. *In vitro*, oxygen enhances direct tumor cell killing at clinically relevant radiation doses (23). The degree of hypoxia required to fully show this phenomenon must be severe (e.g., <5 mm Hg oxygen; ref. 24). Adaptive HIF-1 signaling to hypoxia is elicited at much higher concentrations of oxygen (as high as 40 mm Hg), with additional modulation occurring as oxygen deprivation becomes more pronounced (25). This underscores a more complicated interaction between hypoxia and tumor cell radiation response in whole tumors, in which radiation impacts tumor cell survival both directly and indirectly through effects on stromal cell populations. Tumor cells which successfully adapt to microenvironmental stress are able to co-opt and/or induce stromal blood vessels to enhance their oxygen and nutrient supply by paracrine growth factor signaling (26). HIF-1–stimulated tumor expression of VEGF and other proangiogenic factors is key to this process (27). Given that radiotherapy can damage tumor vascular function and lead to secondary ischemic tumor stress, it is logical to expect tumor cell HIF-1 signaling to serve as an important determinant of whole tumor radiation response. This indeed has been shown (10), although the exact mechanisms responsible for postradiotherapy HIF-1 signaling remain incompletely defined.

Mixed findings have been elicited from *in vitro* studies of HIF-1 tumor cell signaling following radiation (10, 28). Using our functional reporter system, we have shown that tumor HIF-1 signaling responses to irradiation occur exclusively in intact vascularized tumors. Previous data (10) suggest that reoxygenation events are responsible for induction of HIF-1 after irradiation, a phenomenon we did not observe *in vivo*. We directly associated postradiation HIF-1 upregulation with ischemic microenvironmental stress via submicron-resolution, quantitative analysis of IHC images and nondisruptive, submillimeter-resolution multimodality imaging. Thus, our findings implicate an alternative pathophysiologic cascade in which tumor radioresponse and resistance are determined by ischemic tumor cell maintenance of underlying stromal vascular supply. Although physical hypoxia may directly impart tumor cell radioresistance (e.g., reduced concentrations of free radical species), our results show that hypoxia can also impact *in vivo* radioresistance through indirect paracrine mechanisms of stromal vascular maintenance. Absence of supportive paracrine tumor cell signaling during irradiation (such as in normoxic tumor regions) would leave ECs more susceptible to dysfunction and killing from radiation. Thus, in C6 and HN5 tumors, chronically hypoxic yet viable tumor regions contain foci of resistant tumor vessels which themselves serve as the target for postradiation paracrine signaling from surviving tumor cells, leading to stromal revascularization.

Published OnlineFirst March 1, 2011; DOI: 10.1158/1541-7786.MCR-10-0469

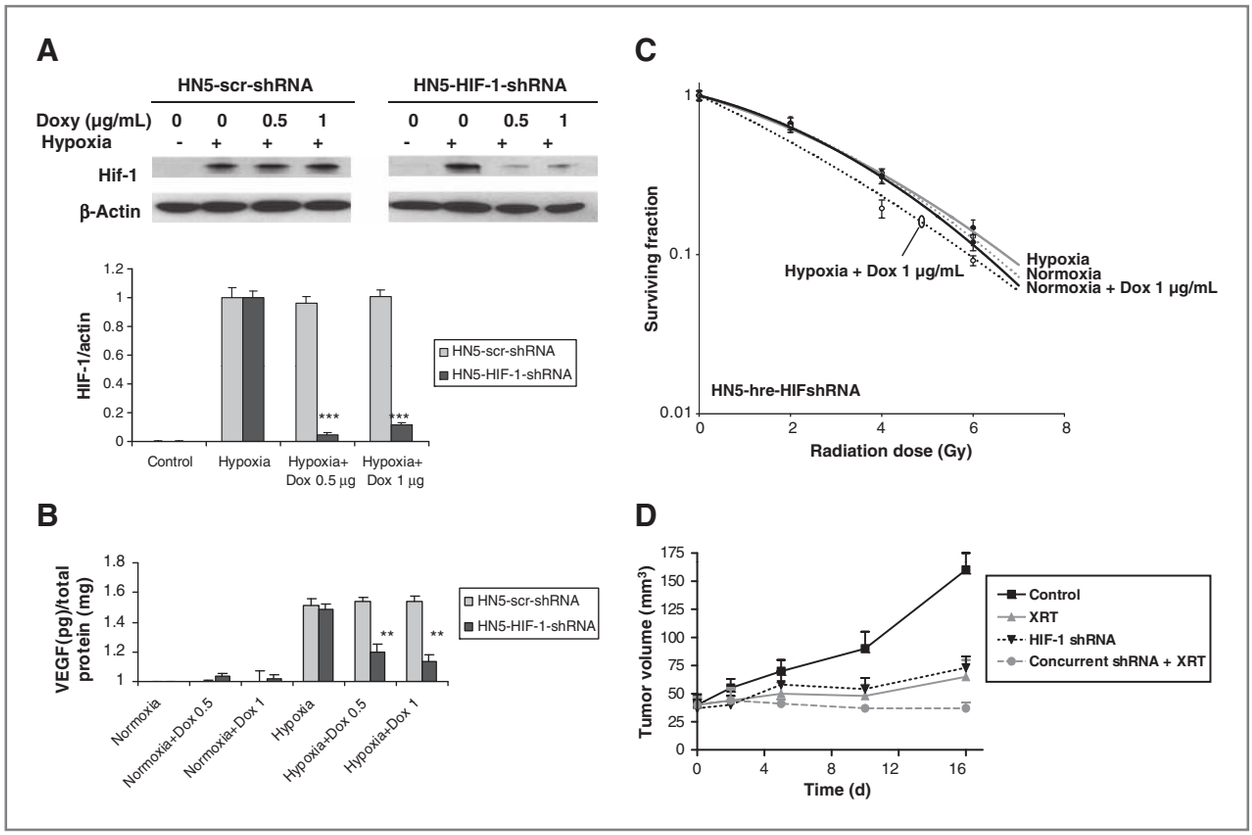

Figure 6. *In vitro* conditional knockdown of HIF-1 and downstream soluble VEGF expression in response to moderate hypoxia were measured by (A) Western blotting and (B) ELISA assays, respectively, in HN5-HIF-1-shRNA cells treated with doxycycline at 0, 0.5, or 1 μg/mL in normoxic conditions in serum-starved (1% FBS) media for 48 hours and then transferred to 1% O_2 for 24 hours with constant doxycycline (Dox) concentration before collection; **, $P < 0.005$; ***, $P < 0.001$. HN5-scr-shRNA, scrambled shRNA controls. C, *in vitro* HN5-HIF-1-shRNA clonogenic survival curves. D, *in vivo* HN5-HIF-1-shRNA xenograft tumor growth.

Our results do not exclude reoxygenation-dependent tumor HIF-1 upregulation events following irradiation, particularly in alternative tumor models with less pronounced baseline VEGF signaling than C6 and HN5. In fact, both reoxygenation and ischemic events could conceivably play complementary roles in tumor adaptation and resistance. However, exact delineation of the respective importance of either mechanism across specific tumor types will have key therapeutic implications, because *early* concurrent HIF-1 inhibition would be expected to optimally treat resistant ischemic tumor regions with chronic tumor HIF-1 signaling. Alternatively, sequencing of HIF-1 blockade *after* radiation would potentially best impact tumors relying on posttreatment reoxygenation to drive adaptive HIF-1 signaling; in fact, data from 4T1 and HCT-116 tumor models directly support this premise (29).

High-resolution small animal imaging is well suited to serially interrogate these mechanisms within intact tumor models. DCE-MRI can quantifiably evaluate integrity and function of tumor microvasculature and also tumor response to antiangiogenic or antivascular therapy (30). The dual-tracer DCE-MRI technique we used differentiates vascular enhancement from rapid extravasation and correlates better with histologic end points than by traditional single-tracer studies (16, 31). Preclinical ultrasonography provides additional quantification of tumor blood flow (32–35). Sophisticated multimodality approaches are required to capitalize on the complementary strengths of such techniques. Pilot reports have shown the feasibility of combined ultrasonography and MRI to assess tumor vessel radiation responses in mouse xenografts (32, 33). Other studies have combined vascular MRI with optical assessment of HIF-1 pathway signaling (36) or with pulsed electron paramagnetic resonance localization of physical hypoxia (37). For this study, we leveraged a multimodality platform utilizing physically immobilized dorsal skin window tumors to obtain high-resolution data with rigorous image coregistration during an extended time course of repetitive imaging. Our studies confirmed expected limitations of this system caused by the discrepancy between MR image resolution (~156 μm in-plane) and the point-spread function of PET (~3 mm). Quantification of baseline voxel-to-voxel correlation of PET signal to T_2^*/R_2^* maps remain difficult to reproduce because of PET resolution limitations and adjacent air–tissue interfaces and tissue heterogeneity. Efforts to improve robustness of quantification are ongoing.

Published OnlineFirst March 1, 2011; DOI: 10.1158/1541-7786.MCR-10-0469

Nonetheless, strong qualitative agreement between PET signal and DCE-MRI parametric maps of low-molecular-weight MR contrast delivery to the extravascular compartment (e.g., Magnevist-dependent permeability maps, Fig. 5) confirmed close spatial association of HIF-1 signaling with postradiation tumor microvessel disruption. Importantly, the lack of correspondence between HIF-1 PET signal and the fraction of tissue volume occupied by vessels (e.g., high-molecular-weight PG-Gd-DTPA contrast–dependent vascular volume fraction maps, Fig. 5) emphasizes the limitations of simple quantified measures of tumor blood vessel density devoid of spatial information.

Targeted inhibition of HIF-1 has been shown both to provide direct antitumor activity (38) and to enhance tumor radiosensitivity (6, 7, 39, 40) in preclinical studies. Selective HIF-1 pharmacologic inhibitors are now entering early clinical development (41, 42). Many questions remain before rationally designed HIF-1–targeted radiosensitization strategies can be optimized for the clinic. HIF-1 knockdown leads to variable effects across cell types and may provide ineffective tumor radiosensitization, or even tumor cell radioprotection. The exact cell population which serves as the functional target of HIF-1 inhibition *in vivo* is not certain. This undoubtedly varies across tumor types and disease sites and may, in fact, be stromal constituents (e.g., tumor vessel endothelium) rather than tumor cells themselves. A genetic loss-of-function study with HIF-1α null ECs showed an HIF-1–driven VEGF-VEGFR2 autocrine loop originating within the endothelium which is required for solid tumor angiogenesis (43), supporting the notion that stromal vasculature could be exploited as a direct target of HIF-1 inhibition. Stromal sensitivity to radiation potentially varies across organ sites, not only due to differences in native radioresistance of ECs but also due to the quality, dynamics, and specific signaling of proteins responsible for supportive paracrine signaling (44). Blouw and colleagues (45) have shown that HIF blockade can lead to increased vessel cooption and tumor cell invasion in vessel-rich brain parenchyma versus less vascularized subcutaneous tissues, further emphasizing critical tissue-specific effects of HIF-1 blockade. Finally, the respective roles played by different members of the HIF-α family, including HIF-2α and HIF-3α, across individual tumor types remain unclear. Despite similarities between HIF-1α and HIF-2α, there is little redundancy between the downstream effects of these two proteins (46, 47). Nonetheless, we have found HIF-2 to be only weakly expressed in C6 and HN5 xenografts (<10% expression by immunohistochemistry at baseline and postradiation; data not shown), supporting the primacy of HIF-1–specific adaptive signaling in these models.

Conclusions

Our results show a stroma-dependent cascade responsible for whole tumor radioresistance. Radiosensitivity and kinetics of postradiation vascular recovery depend on HIF-1–mediated paracrine prosurvival signaling from nutrient-deprived, hypoxic tumor cells to stromal vasculature. Poorly perfused regions in which tumor cells produce higher levels of proangiogenic factors selectively protect neighboring microvessels from radiation insult. Tumor regions with normal perfusion and lower levels of proangiogenic factors are more sensitive to radiation-induced vascular dysfunction. The degree of ischemic HIF-1 signal stimulation determines the magnitude of adaptive proangiogenic signaling from tumor cells to regain stromal support. Therefore, targeted HIF-1 blockade promises effective inhibition of the signaling source for whole tumor adaptation events. *In situ* spatiotemporal imaging promises to clarify the respective roles of constituent tumor subpopulations and the temporal dynamics of adaptive postradiation responses. This information can potentially guide rational administration of targeted radiosensitizing agents and streamline downstream deployment of such strategies into the clinical trial setting.

Disclosure of Potential Conflicts of Interest

N. Kuno is an employee of Hitachi Ltd. G. Powis owns stock in Oncothyreon, which owns PX-478.

Acknowledgments

We thank Drs. Benjamin Moeller and Dominique Jennings for their expertise and assistance with MRI-compatible dorsal skin window platform development.

Grant Support

The work was supported by the Experimental Cancer Imaging Research Program (U24-CA126577), NIH grants CA017094 to G. Powis and D. L. Schwartz, NIH grants CA095060, CA098920, and CA1019552 to G. Powis, New Program Development Funds and faculty startup funding from the Department of Experimental Diagnostic Imaging to J. Gelovani and M. Alauddin, and the Cancer Center Support Grant (P30-CA016672) at M.D. Anderson. D. Schwartz received support from the University of Texas Inter-Institutional Biomedical Engineering Program and grant-in-aid funding from Hitachi Ltd.

The costs of publication of this article were defrayed in part by the payment of page charges. This article must therefore be hereby marked *advertisement* in accordance with 18 U.S.C. Section 1734 solely to indicate this fact.

Received October 19, 2010; revised January 11, 2011; accepted January 14, 2011; published online March 1, 2011.

References

1. Brizel DM, Scully SP, Harrelson JM, Layfield LJ, Bean JM, Prosnitz LR, et al. Tumor oxygenation predicts for the likelihood of distant metastases in human soft tissue sarcoma. Cancer Res 1996;56:941–3.
2. Hockel M, Schlenger K, Aral B, Mitze M, Schaffer U, Vaupel P. Association between tumor hypoxia and malignant progression in advanced cancer of the uterine cervix. Cancer Res 1996;56:4509–15.
3. Nordsmark M, Overgaard J. A confirmatory prognostic study on oxygenation status and loco-regional control in advanced head and neck squamous cell carcinoma treated by radiation therapy. Radiother Oncol 2000;57:39–43.
4. Semenza GL. HIF-1: mediator of physiological and pathophysiological responses to hypoxia. J Appl Physiol 2000;88:1474–80.

Published OnlineFirst March 1, 2011; DOI: 10.1158/1541-7786.MCR-10-0469

5. Semenza GL. Targeting HIF-1 for cancer therapy. Nat Rev Cancer 2003;3:721–32.
6. Schwartz DL, Powis G, Thitai-Kumar A, He Y, Bankson J, Williams R, et al. The selective hypoxia inducible factor-1 inhibitor PX-478 provides *in vivo* radiosensitization through tumor stromal effects. Mol Cancer Ther 2009;8:947–58.
7. Schwartz DL, Bankson JA, Lemos R Jr, Lai SY, Thittai AK, He Y, et al. Radiosensitization and stromal imaging response correlates for the HIF-1 inhibitor PX-478 given with or without chemotherapy in pancreatic cancer. Mol Cancer Ther 2010;9:2057–67.
8. Carmeliet P. Angiogenesis in life, disease and medicine. Nature 2005;438:932–6.
9. Kakeji Y, Maehara Y, Ikebe M, Teicher BA. Dynamics of tumor oxygenation, CD31 staining and transforming growth factor-beta levels after treatment with radiation or cyclophosphamide in the rat 13762 mammary carcinoma. Int J Radiat Oncol Biol Phys 1997;37:1115–23.
10. Moeller BJ, Cao Y, Li CY, Dewhirst MW. Radiation activates HIF-1 to regulate vascular radiosensitivity in tumors: role of reoxygenation, free radicals, and stress granules. Cancer Cell 2004;5:429–41.
11. Wen B, Burgman P, Zanzonico P, O'donoghue J, Cai S, Finn R, et al. A preclinical model for noninvasive imaging of hypoxia-induced gene expression; comparison with an exogenous marker of tumor hypoxia. Eur J Nucl Med Mol Imaging 2004;31:1530–8.
12. Serganova I, Doubrovin M, Vider J, Ponomarev V, Soghomonyan S, Beresten T, et al. Molecular imaging of temporal dynamics and spatial heterogeneity of hypoxia-inducible factor-1 signal transduction activity in tumors in living mice. Cancer Res 2004;64:6101–8.
13. Alauddin MM, Conti PS, Fissekis JD. A general synthesis of [18F] labeled 2′-deoxy-2′-fluoro-1-β-D-arabinofuranosyluracil nucleosides. J Labelled Comp Radiopharm 2003;46:285–9.
14. Daldrup H, Shames DM, Wendland M, Okuhata Y, Link TM, Rosenau W, et al. Correlation of dynamic contrast-enhanced MR imaging with histologic tumor grade: comparison of macromolecular and small-molecular contrast media. AJR Am J Roentgenol 1998;171:941–9.
15. Tofts PS. Modeling tracer kinetics in dynamic Gd-DTPA MR imaging. J Magn Reson Imaging 1997;7:91–101.
16. Weissleder R, Cheng HC, Marecos E, Kwong K, Bogdanov A Jr. Non-invasive *in vivo* mapping of tumour vascular and interstitial volume fractions. Eur J Cancer 1998;34:1448–54.
17. Wen X, Jackson EF, Price RE, Kim EE, Wu Q, Wallace S, et al. Synthesis and characterization of poly(l-glutamic acid) gadolinium chelate: a new biodegradable MRI contrast agent. Bioconjug Chem 2004;15:1408–15.
18. Maes F, Collignon A, Vandermeulen D, Marchal G, Suetens P. Multimodality image registration by maximization of mutual information. IEEE Trans Med Imaging 1997;16:187–98.
19. Bidaut LM, Pascual-Marqui R, Delavelle J, Naimi A, Seeck M, Michel C, et al. Three- to five-dimensional biomedical multisensor imaging for the assessment of neurological (dys)function. J Digit Imaging 1996;9:185–98.
20. Nordsmark M, Alsner J, Keller J, Nielsen OS, Jensen OM, Horsman MR, et al. Hypoxia in human soft tissue sarcomas: adverse impact on survival and no association with p53 mutations. Br J Cancer 2001;84:1070–5.
21. Hockel M, Schlenger K, Mitze M, Schaffer U, Vaupel P. Hypoxia and radiation response in human tumors. Semin Radiat Oncol 1996;6:3–9.
22. Tatum JL, Kelloff GJ, Gillies RJ, Arbeit JM, Brown JM, Chao KS, et al. Hypoxia: importance in tumor biology, noninvasive measurement by imaging, and value of its measurement in the management of cancer therapy. Int J Radiat Biol 2006;82:699–757.
23. Palcic B, Skarsgard LD. Reduced oxygen enhancement ratio at low doses of ionizing radiation. Radiat Res 1984;100:328–39.
24. Hall EJ, Giaccia AJ. Radiobiology for the Radiologist. 6th ed. Philadelphia, PA: Lippincott Williams & Wilkins; 2004.
25. Pouyssegur J, Dayan F, Mazure NM. Hypoxia signalling in cancer and approaches to enforce tumour regression. Nature 2006;441:437–43.
26. Joyce JA. Therapeutic targeting of the tumor microenvironment. Cancer Cell 2005;7:513–20.
27. Pugh CW, Ratcliffe PJ. Regulation of angiogenesis by hypoxia: role of the HIF system. Nat Med 2003;9:677–84.
28. Kim WY, Oh SH, Woo JK, Hong WK, Lee HY. Targeting heat shock protein 90 overrides the resistance of lung cancer cells by blocking radiation-induced stabilization of hypoxia-inducible factor-1alpha. Cancer Res 2009;69:1624–32.
29. Moeller BJ, Dreher MR, Rabbani ZN, Schroeder T, Cao Y, Li CY, et al. Pleiotropic effects of HIF-1 blockade on tumor radiosensitivity. Cancer Cell 2005;8:99–110.
30. Jackson A, O'Connor JP, Parker GJ, Jayson GC. Imaging tumor vascular heterogeneity and angiogenesis using dynamic contrast-enhanced magnetic resonance imaging. Clin Cancer Res 2007;13:3449–59.
31. Orth RC, Bankson J, Price R, Jackson EF. Comparison of single- and dual-tracer pharmacokinetic modeling of dynamic contrast-enhanced MRI data using low, medium, and high molecular weight contrast agents. Magn Reson Med 2007;58:705–16.
32. Yankeelov TE, Niermann KJ, Huamani J, Kim DW, Quarles CC, Fleischer AC, et al. Correlation between estimates of tumor perfusion from microbubble contrast-enhanced sonography and dynamic contrast-enhanced magnetic resonance imaging. J Ultrasound Med 2006;25:487–97.
33. Niermann KJ, Fleischer AC, Huamani J, Yankeelov TE, Kim DW, Wilson WD, et al. Measuring tumor perfusion in control and treated murine tumors: correlation of microbubble contrast-enhanced sonography to dynamic contrast-enhanced magnetic resonance imaging and fluorodeoxyglucose positron emission tomography. J Ultrasound Med 2007;26:749–56.
34. Fentzke RC, Korcarz CE, Lang RM, Lin H, Leiden JM. Dilated cardiomyopathy in transgenic mice expressing a dominant-negative CREB transcription factor in the heart. J Clin Invest 1998;101:2415–26.
35. Mor-Avi V, Korcarz C, Fentzke RC, Lin H, Leiden JM, Lang RM. Quantitative evaluation of left ventricular function in a transgenic mouse model of dilated cardiomyopathy with 2-dimensional contrast echocardiography. J Am Soc Echocardiogr 1999;12:209–14.
36. Raman V, Artemov D, Pathak AP, Winnard PT Jr, McNutt S, Yudina A, et al. Characterizing vascular parameters in hypoxic regions: a combined magnetic resonance and optical imaging study of a human prostate cancer model. Cancer Res 2006;66:9929–36.
37. Matsumoto S, Hyodo F, Subramanian S, Devasahayam N, Munasinghe J, Hyodo E, et al. Low-field paramagnetic resonance imaging of tumor oxygenation and glycolytic activity in mice. J Clin Invest 2008;118:1965–73.
38. Kung AL, Wang S, Klco JM, Kaelin WG, Livingston DM. Suppression of tumor growth through disruption of hypoxia-inducible transcription. Nat Med 2000;6:1335–40.
39. Williams KJ, Telfer BA, Xenaki D, Sheridan MR, Desbaillets I, Peters HJ, et al. Enhanced response to radiotherapy in tumours deficient in the function of hypoxia-inducible factor-1. Radiother Oncol 2005;75:89–98.
40. Kioi M, Vogel H, Schultz G, Hoffman RM, Harsh GR, Brown JM. Inhibition of vasculogenesis, but not angiogenesis, prevents the recurrence of glioblastoma after irradiation in mice. J Clin Invest 2010;120:694–705.
41. Powis G, Kirkpatrick L. Hypoxia inducible factor-1 alpha as a cancer drug target. Mol Cancer Ther 2004;3:647–54.
42. Belozerov VE, Van Meir EG. Hypoxia inducible factor-1: a novel target for cancer therapy. Anticancer Drugs 2005;16:901–9.
43. Tang N, Wang L, Esko J, Giordano FJ, Huang Y, Gerber HP, et al. Loss of HIF-1alpha in endothelial cells disrupts a hypoxia-driven VEGF autocrine loop necessary for tumorigenesis. Cancer Cell 2004;6:485–95.
44. Ryan HE, Poloni M, McNulty W, Elson D, Gassmann M, Arbeit JM, et al. Hypoxia-inducible factor-1alpha is a positive factor in solid tumor growth. Cancer Res 2000;60:4010–5.
45. Blouw B, Song H, Tihan T, Bosze J, Ferrara N, Gerber HP, et al. The hypoxic response of tumors is dependent on their microenvironment. Cancer Cell 2003;4:133–46.
46. Wenger RH. Cellular adaptation to hypoxia: O_2-sensing protein hydroxylases, hypoxia-inducible transcription factors, and O_2-regulated gene expression. FASEB J 2002;16:1151–62.
47. Wang V, Davis DA, Haque M, Huang LE, Yarchoan R. Differential gene up-regulation by hypoxia-inducible factor-1alpha and hypoxia-inducible factor-2alpha in HEK293T cells. Cancer Res 2005;65:3299–306.

Published OnlineFirst March 1, 2011; DOI: 10.1158/1541-7786.MCR-10-0469

Molecular Cancer Research

HIF-1–Dependent Stromal Adaptation to Ischemia Mediates *In Vivo* Tumor Radiation Resistance

David L. Schwartz, James Bankson, Luc Bidaut, et al.

Mol Cancer Res 2011;9:259-270. Published OnlineFirst March 1, 2011.